HHS Public Access

Author manuscript

Magn Reson Med. Author manuscript; available in PMC 2022 February 01.

Published in final edited form as:

Magn Reson Med. 2021 February ; 85(2): 953–961. doi:10.1002/mrm.28447.

Cerebral oxygen extraction fraction (OEF): comparison of dual-gas challenge calibrated BOLD with CBF and challenge-free gradient echo QSM+qBOLD

Junghun Cho[1], **Yuhan Ma**[2], **Pascal Spincemaille**[1], **G. Bruce Pike**[2,4], **Yi Wang**[1,3]

[1]Department of Radiology, Weill Cornell Medical College, New York, New York, USA

[2]McConnell Brain Imaging Centre, Montreal Neurological Institute, McGill University, Montreal, Canada

[3]Department of Biomedical Engineering, Cornell University, Ithaca, New York, USA

[4]Department of Radiology and Hotchkiss Brain Institute, University of Calgary, Calgary, Canada

Abstract

Purpose: To compare cortical gray matter OEF estimated from two MRI methods: 1) the quantitative susceptibility mapping plus quantitative blood oxygen level-dependent magnitude (QSM+qBOLD or QQ) and 2) the dual-gas calibrated-BOLD (DGCB) in healthy subjects, and to investigate the validity of iso-$CMRO_2$ assumption during hypercapnia using QQ.

Methods: In ten healthy subjects, 3T MRI including a multi-echo GRE sequence at baseline and hypercapnia for QQ, as well as an EPI dual-echo pseudo-continuous arterial spin labeling (pCASL) for DGCB were performed under a hypercapnic and a hyperoxic condition. OEFs from QQ and DGCB were compared using ROI analysis and paired t-test. For QQ, $CMRO_2$=CBF*OEF*Ca (Ca=arterial oxygen content) was generated for both baseline and hypercapnia, which were compared.

Results: Average OEF in cortical gray matter (CGM) across 10 subjects from QQ vs DGCB were 35.5 ± 6.7 vs 38.0 ± 9.1 % (P=0.49) at baseline; and 20.7 ± 4.4 vs 28.4 ± 7.6 % (P=0.02) in hypercapnia: OEF in CGM was significantly reduced as measured in QQ (P<0.01) and in DGCB (P<0.01). $CMRO_2$ (in μmol O_2/min/100g) was 168.2 ± 54.1 at baseline from DGCB; and 153.1 ± 33.8 at baseline and 126.4 ± 34.2 (P<0.01) in hypercapnia from QQ.

Conclusions: The differences in OEF obtained from QQ and DGCB are small and non-significant at baseline, but are statistically significant during hypercapnia. In addition, QQ shows a $CMRO_2$ decrease (17.4%) during hypercapnia.

Corresponding author: Yi Wang, Cornell MRI, 515 East 71st St, Suite 102, New York, NY 10021, USA, Phone: (646) 962-2631, yiwang@med.cornell.edu.

Data Availability Statement: The code that supports the findings of this study will be openly available at http://pre.weill.cornell.edu/mri/.

Keywords

oxygen extraction fraction; OEF; cerebral metabolic rate of oxygen; $CMRO_2$; quantitative susceptibility mapping; QSM; quantitative blood oxygenation level-dependent imaging; qBOLD; QSM+qBOLD; QQ; dual-gas calibrated BOLD; DGCB

INTRODUCTION

Cerebral metabolic rate of oxygen consumption ($CMRO_2$) and oxygen extraction fraction (OEF) are essential biomarkers for tissue viability and function, and are thought to be altered in various diseases, such as stroke (1–4), tumor (5), and Alzheimer's Disease (6). In MRI, a variety of quantitative models have been proposed to estimate $CMRO_2$ and OEF either from 1) MR magnitude signal, such as quantitative BOLD (qBOLD) (7,8), quantitative imaging of extraction of oxygen and tissue consumption (QUIXOTIC) (9), and calibrated BOLD (10–13), or 2) MR phase signal, including whole brain susceptometry-based oximetry (14,15) as well as macrovascular (16–18) and microvascular (19–21) OEF quantification using quantitative susceptibility mapping (QSM) methods.

Calibrated BOLD is a quantitative modeling of deoxyhemoglobin concentration [dHb] using the MR magnitude signal (13). It isolates the $CMRO_2$ contribution from the BOLD signal, a complex function of cerebral blood flow (CBF), cerebral blood volume (CBV), and $CMRO_2$, with the aid of respiratory challenges. When a single respiratory challenge is used, relative $CMRO_2$ change associated with a task can be quantified. With more than one respiratory challenge, such as dual-gas calibrated BOLD (DGCB) that combines hypercapnia and hyperoxia, baseline absolute $CMRO_2$ can be estimated. In step-wise DGCB, the maximum BOLD response, M, can be obtained first from hypercapnia with an iso-$CMRO_2$ assumption. With the obtained M, the baseline OEF is then estimated based on BOLD and CBF changes under hyperoxia (12,22).

On the other hand, the QSM-based microvascular OEF method is a quantitative modeling of [dHb] using MR phase signal (19–21). QSM modeling of biological iron (23,24) forms allows extraction of [dHb] contribution from the voxel-wise susceptibility values by employing a vascular challenge (19,21,25), using a local minimization method (20), or combining with qBOLD (QSM+qBOLD or QQ) for a comprehensive modeling on both magnitude and phase of multi-echo gradient echo (mGRE) data (26). QQ can quantify OEF and $CMRO_2$ without vascular challenges, hence it is more practical in a clinical setting. The robustness of QQ against measurement noise can be further improved with cluster analysis of time evolution (CAT) (27).

In this study, we aim to cross-validate QQ-CAT with DGCB for OEF measurement in cortical gray matter in healthy subjects. In addition, because QQ does not require a vascular challenge, it can measure OEF at both baseline and hypercapnia independently. Hence, we investigate the debated assumption that $CMRO_2$ is unchanged during hypercapnia, which is of great interest for future calibrated BOLD studies.

METHODS

Data Acquisition

MRI was performed in 10 healthy subjects (5 female subjects, age 29 ± 5 years) on a Siemens Tim Trio 3 T scanner with a 32-channel RF receiver head coil after providing informed written consent. The study was approved by the Research Ethics Board of the Montreal Neurological Institute and Hospital.

For QQ data, a 3D MPRAGE sequence with 1 mm^3 voxel size was used to acquire an anatomical image. A 3D multi-echo gradient echo (mGRE) sequence with flow compensation along all three axes was used to generate quantitative susceptibility maps (28). The 3D mGRE sequence parameters were: 1 mm in-plane resolution, 1 mm slice thickness, 7 equally spaced echoes: $TE_1/\Delta TE/TE_7$ = 4.6/4.06/29.0 ms, TR= 32 ms, monopolar readouts with a bandwidth of 977 Hz/pixel, flip angle 20°, GRAPPA acceleration factor = 2, phase partial Fourier = 3/4. The mGRE complex images from all 32 channels were combined using the singular value decomposition method to avoid the open-ended fringeline (29). GRE data were acquired at baseline and during a hypercapnic condition to prospectively target partial pressure of end-tidal CO_2 ($PetCO_2$) to 7 mmHg above the participant's baseline using a computerized gas-delivery system RespirAct (Thornhill Research Inc., Toronto, ON, Canada).

DGCB data were collected using an EPI dual-echo pseudo-continuous arterial spin labeling (pCASL) sequence with $TR/TE_1/TE_2$ = 4000/10/30 ms, voxels = 3.9 mm isotropic, label duration = 1665, post-label delay = 900/1568/2235 ms (first/center/last slice), GRAPPA = 2, phase partial Fourier =7/8, 25 slices, labelling location =10 cm below the central slice, and descending slice acquisition order. For quantifying resting CBF and OEF, dual-echo pCASL data were acquired under a baseline condition, a hypercapnic challenge condition, and two hyperoxic conditions. Gas manipulations were achieved with the RespirAct system. For hypercapnia, an increased $PetCO_2$ of 7 mmHg above participant's baseline was targeted (56 s baseline, 56 s hypercapnia, 120 s baseline, 120 s hypercapnia and 56 s baseline) while 102 volumes of pCASL EPI data were acquired with an acquisition time of 7 mins. Hyperoxic gas manipulation aimed to increase $PetO_2$ by 150 mmHg and 300 mmHg above participant's baseline (120 s baseline, 120 s of $PetO_2$ +150 mmHg hyperoxia, 120 s of $PetO_2$ +300 mmHg hyperoxia, and 56 s baseline). 120 volumes of pCASL EPI data were acquired during hyperoxia with an acquisition time of 8 mins and 12 seconds.

For each subject, the arterial oxygenation, Y_a, was measured with a pulse oximeter (Oxyn Vantage, Nonin Medical Inc.) and heme molar concentration [H] was obtained with performing complete blood count on forearm blood sample.

Data processing

CBF quantification from ASL data: pCASL data were processed with the SPM8 ASLtbx for baseline CBF calculation. Baseline CBF was then registered and resampled to QSM resolution. CBF cerebrovascular reactivity (CVR), i.e. the fractional CBF change induced by unit $PetCO_2$, maps were calculated using the pCASL hypercapnia data. The CVR maps were then multiplied by the measured $PetCO_2$ during hypercapnia QSM

acquisitions and added to the baseline CBF to infer CBF during hypercapnic QSM acquisitions.

QQ OEF and $CMRO_2$ mapping from GRE data at baseline and at hypercapnia separately: The OEF map was estimated by the QQ model, consisting of QSM of phase and qBOLD of magnitude of mGRE data as detailed in (27). QSM reconstruction was performed as follows: first, a linear fit of the mGRE phase was performed to estimate the total field (30). Second, the Laplacian boundary value (LBV) was used to obtain the local field (31). Finally, Morphology Enabled Dipole Inversion with automatic uniform cerebrospinal fluid zero reference (MEDI+0) algorithm was used to compute susceptibility (32–37). The mGRE magnitude was modeled according to qBOLD and further denoised according to the cluster analysis of time evolution (CAT) by following the approach outlined by Cho et al. (27) with incorporating tissue type information by tripling the number of clusters into gray matter (GM), white matter (WM), cerebrospinal fluid (CSF) clusters and without the OEF regularization in the QQ-CAT optimization. The cluster-specific v values are initialized to be 4/2/0% for GM/WM/CSF clusters. The GM/WM/CSF segmentation is performed by FSL FAST (38) with the echo-combined magnitude image of mGRE. The straight sinus mask in the processing was obtained automatically using global and regional thresholding on QSM combined with positional (inferior, posterior brain) and geometrical (straightness of the vein) constraints at baseline as described in (27) and was visually checked. For hypercapnia, the straight sinus mask at baseline was registered using the FSL FLIRT algorithm (39,40).

DGCB OEF mapping at baseline and hypercapnia and $CMRO_2$ assumed invariant during hypercapnia: DGCB data were analyzed as detailed in (25). The steady-state values of $PetCO_2$ and $PetO_2$ were obtained via linear regression on the entire hypercapnic ($PetCO_2$) and hyperoxia ($PetO_2$) run, respectively. The steady-state end-tidal values were then used to form boxcar functions and convolved with a single gamma function (standard deviation of 20 s and mean lag time of 40 s) to be used as regressors for BOLD and CBF modeling in the general linear model (GLM) using FSL FEAT (39–43). For BOLD data, an additional linear and zig-zag regressor was included to account for linear signal drift and for the tag and control signal differences, respectively. For CBF data, first echo of pCASL data were sinc subtracted and low-pass filtered with cut-off frequency of 0.125 Hz to filter out high-frequency noise prior to GLM. For BOLD data during the hyperoxic run, the end-tidal CO_2 trace was included as an additional regressor to reduce the influence of any CO_2 changes on BOLD responses because small increases in end-tidal CO_2 temporarily occurred during transitions of hyperoxia challenges. From the GLM analysis, the percentage signal changes of BOLD and CBF associated with hypercapnia were extracted and used to calculate M according to the Davis model (44). The hyperoxic BOLD fractional signal change at $PetO_2$ = +300 mmHg was extracted from GLM. Because of the low SNR in pCASL scans, the percentage signal changes of CBF associated with hyperoxia (+300 mmHg $PetO_2$) were assumed to be −3.11% as suggested in (12). Baseline OEF values were then derived from M, hyperoxia BOLD and CBF changes according to Bulte et al. (22). The OEF in hypercapnia was calculated with 1) the baseline OEF, 2) baseline CBF, and 3) hypercapnia CBF based on the iso-$CMRO_2$ assumption.

ROI analysis

Comparisons of OEF measures between QQ-OEF and DGCB-OEF were performed in cortical gray matter (CGM). The CGM was automatically segmented using the atlas derived from (45), and retaining the voxel with 1) significant BOLD and CBF responses to hypercapnia and significant BOLD responses to hyperoxia ($z > 2.3$), 2) plausible OEF (from 0 to 1), and 3) realistic $CMRO_2$ (from 0 to 1000). For ROI analysis of the QQ result, the obtained CGM mask was resampled to the QSM data resolution and overlapped with the GM mask made in the QSM resolution using FSL FAST (38) with the echo-combined magnitude image from mGRE. Histograms of OEF values were computed and compared between methods.

RESULTS

Hypercapnia gas manipulations resulted in the end-tidal CO_2 increase in all subjects. Close to the targeted $PetCO_2$ (+7 mmHg), average $PetCO_2$ increase was 5.8 ± 1.2 and 6.3 ± 1.0 mmHg for the calibrated BOLD scans and for QSM scans, respectively. $PetCO_2$ increase between the two methods were not significantly different (P=0.2). Hyperoxia gas manipulations increased $PetO_2$ in all subjects for an average end-tidal O_2 increase of 277.1 ± 23.7 mmHg for the targeted $PetO_2$ = +300 mmHg.

Figure 1 shows OEF maps in two subjects at baseline (BL) and hypercapnia (HC) for DGCB and QQ. Compared to DGCB, QQ showed more uniform OEF. At BL, QQ showed similar average OEF values compared to DGCB in CGM (Table 1) (N=10): 35.5 ± 6.7 and 38.0 ± 9.1 % (P=0.49). However, for HC, QQ showed lower OEF values than DGCB (Table 1): 20.7 ± 4.4 vs 28.4 ± 7.6 % (P=0.02). Compared to BL, HC showed significantly reduced OEF in CGM for both QQ (P<0.01) and DGCB (P<0.01).

Figure 2 shows $CMRO_2$ and CBF in the same two subjects at BL and HC for DGCB and QQ. QQ showed a good $CMRO_2$ contrast between gray and white matter without extremely high values. At BL, the QQ estimated $CMRO_2$ was not significantly different than that obtained with DGCB in CGM (Table 1): 153.1 ± 33.8 and 168.2 ± 54.1 μmol O_2/min/100g (P=0.36). In HC, QQ showed lower $CMRO_2$ compared to BL: 126.4 ± 34.2 μmol O_2/min/100g (P<0.01). Note that HC-$CMRO_2$ is identical to BL-$CMRO_2$ in DGCB (iso-$CMRO_2$ assumption). In addition, higher CBF and venous blood volume (v) were measured during HC compared to BL (Table 2): 82.4 ± 11.8 vs 56.8 ± 9.8 ml/min/100g (P<0.01) for CBF and 3.1 ± 0.5 vs. 2.8 ± 0.4 % (P=0.35) for v (Supporting Information Figure S3). Histograms of OEF values for QQ and DBCB in two subjects are shown in Figure S4 in Supporting Information.

Hypercapnia gas manipulations increased gray matter CBF and BOLD signals in all subjects, on average, 38.6 ± 7.4 % for CBF and 2.3 ± 0.5 % for BOLD. Average CBF cerebrovascular reactivity (CVR) in gray matter was 7.3 ± 1.8 Δ%CBF/mmHg $PetCO_2$ (Table 2).

DISCUSSION

In this study, the QSM+qBOLD (QQ) OEF mapping method without challenge was compared with dual gas calibrated BOLD (DGCB) OEF mapping and was used to evaluate $CMRO_2$ change during hypercapnia. Although the DGCB is not a gold standard technique for baseline OEF measurement, it is the first established quantitative OEF technique in MRI. Our results indicate that QQ model provided similar OEF values in CGM compared to the DGCB at baseline. Based on this validation, the advantages of QQ, e.g. OEF estimation without a gas inhalation challenge, enables the application of QQ in clinical settings. Furthermore, because no challenge was required, QQ was able to quantify OEF and $CMRO_2$ values independently at baseline and during hypercapnia. QQ showed a 17.4% $CMRO_2$ decrease during hypercapnia. This observation is an important contribution to the debate surrounding the iso-$CMRO_2$ assumption employed in hypercapnia calibrated BOLD studies. The QQ method provides a framework to probe this issue further (e.g. graded hypo- and hypercapnia) and to determine the effects of oxygen manipulations on $CMRO_2$.

Baseline OEF in CGM estimated with the two methods were similar and statistically not significantly different (Table 1): 35.5 ± 6.7 and 38.0 ± 9.1 % (P=0.49) for QQ and DGCB, respectively. Both OEF values fell within the range previously reported using PET: 35 ± 7 % (46) and 40 ± 9 % (47), using calibrated BOLD: 35 ± 4 – 44 ± 14 % (Table 3 in (25)), and using QSM: 29 ± 3 – 50 ± 5 % (Table 4 in (25)).

Compared to the QQ OEF, the DGCB OEF showed greater inter-subject variation (coefficient of variation in CGM = 19% for QQ vs 24% for DGCB), though their group averages at baseline were close (Figure 1 and Table 1). A similar inter-subject variation was also shown in a previous DGCB study (12), and may be attributed to low SNR in BOLD and, in particular, CBF signals in DGCB measurement. Employing an additional gas manipulation such as carbogen might help to decrease the inter-subject variability (48). On the other hand, the small OEF variation in QQ (Figures 1 and 2 and Table 1) may have benefited from the usage of cluster analysis of time evolution (CAT) which improves SNR effectively.

QQ results in relatively uniform OEF values in gray and white matter (Figure 1), which agrees well with previous PET studies (47,49,50). For DGCB, the OEF image quality is visually much more variable than the QQ OEF maps (Figure 1). The DGCB OEF map is not valid in white matter due to the low and very low SNR in the white matter BOLD and CBF measurements, respectively.

The OEF in CGM during hypercapnia from the two methods were different (Table 1): 20.7 ± 4.4 and 28.4 ± 7.6 % (P=0.02) for QQ and DGCB, respectively. The higher OEF in DGCB may be due to the fact that it was estimated using iso-$CMRO_2$ assumption. QQ showed a $CMRO_2$ decrease during hypercapnia compared to baseline, leading to lower hypercapnia OEF with QQ than DGCB, with the same level of CBF (Tables 1 and 2). $CMRO_2$ decrease with hypercapnia is consistent with a $CMRO_2$ increase with hypocapnia (51). However, hypercapnia may involve multiple mechanisms affecting cerebral metabolic activity with their net effects on $CMRO_2$ dependent on the brain condition and region. Decreases,

increases and no significant change in $CMRO_2$ during hypercapnia has been reported in literature (52–55). However, in calibrated BOLD, $CMRO_2$ is often assumed to be unchanged during hypercapnia (13). Because QQ quantifies OEF independently at baseline and hypercapnia, the discrepancy on $CMRO_2$ assumption was further investigated in this study. With a moderate hypercapnia gas manipulation (targeted $PetCO_2$ =+7 mmHg) used in this study, QQ showed a 17.4% $CMRO_2$ reduction in CGM. This is in line with a recent study suggesting 10~15 % reduction with the similar hypercapnic level (55). The QQ model showed significantly lower OEF in hypercapnia (Figures 1 and 2 and Table 1) than baseline, which is consistent with the calibrated BOLD literature (10,44). Future calibrated BOLD studies could include this mild reduction of $CMRO_2$ induced by hypercapnia in its model.

In this study, the v values in CGM were increased under hypercapnia compared to baseline, 2.8 ± 0.4 vs. 3.1 ± 0.5 % (Table 2 and Supporting Information Figure S3). This suggest that the v estimated from QQ-CAT may be sensitive to the physiological difference between baseline (BL) and hypercapnia (HC), as well as OEF. However, the v increase at HC compared to BL is not statistically significant (P=0.35) and greater (11%) than the expected v increase (7%) based on the Grubb relationship: rv (the v ratio between HC and BL) = $rCBF^{0.18}$ (56). The v uncertainty might be related to that the v outcome from QQ-CAT is approximately four times more sensitive to errors including noise than the OEF output. The sensitivity of OEF to the v bias was investigated by processing HC with setting HC-v to the expected value, rv × BL-v. The resultant OEF with using the Grubb relationship for v was not significantly different from the OEF value in this study, 19.8 ± 3.4 vs. 20.7 ± 4.4 (P=0.21). This suggests that OEF is not that sensitive to the v bias.

This study has a number of limitations. First, the results for both DGCB and QQ may be affected by the partial volume effect of vasculatures with tissue and large veins. In QQ, qBOLD model may be inadequate for large veins, which may be handled by imposing 100% venous blood volume at those voxels fully occupied by veins. The partial volume effect may be more severe in DGCB due to lower resolution than QQ (isotropic 3.9 mm vs 1.0 mm). Hence, for ROI analysis, venous blood voxels with large BOLD signal increases (> 10 %) during hypercapnia were excluded in DGCB data. The same mask was also used for QQ to avoid overestimation of OEF. Second, the DGCB OEF results and all CMRO2 reported here may be affected errors in cerebral blood flow measured by PCASL. There was a potentially decreased tagging efficiency in PCASL due to increased blood flow during hypercapnia. This would lead to underestimation in fractional CBF change, which causes OEF overestimation in DGCB. With the hypercapnic levels in this study, tagging efficiency can be reduced by 9% (57), leading to a 9% underestimation in the fractional CBF change, then a 6% overestimation in OEF. With taking this into account, the adjusted average OEF in CGM measured by DGCB would be 35.7%, which agrees well with that measured by QQ (35.5%). This source of error may be mitigated by employing an additional phase-contrast scan to measure the flow velocity in feeding arteries at baseline and during hypercapnia for an accurate assessment of tagging efficiency on a subject-by-subject basis. There were a range of post-label delays used our 2D PCASL acquisition: the first slice was acquired with a post-label delay (PLD) of 900 ms; the centre slice was acquired with a PLD of 1568 ms, close to the recommended 1800 ms PLD. The slightly shorter PLD was selected to accommodate the hypercapnic acquisitions in which arterial transit time was known to decrease. In addition, to

avoid overestimating CBF in macrovascular structures, possibly due to the short PLD, we excluded large arteries that showed larger reductions of CBF during hyperoxia (more than 50 mL/100g/min) due to the T1-shortening by dissolved oxygen in arterial blood plasma and vessel constriction. The CBF values in the final ROIs are 15 ~ 99 mL/100g/min with an average of 55 mL/100g/min, which agrees the expected GM CBF range of healthy subjects. Finally, $CMRO_2$ change during hyperoxia in patients remains to be investigated by QQ in the future, but it is beyond the scope of this study.

In conclusion, our study cross-validated QQ model with the established DGCB. DGCB and QQ OEF values were in agreement for baseline conditions with QQ showing a lower inter-subject variability. Furthermore, QQ results showed a mild (17.4%) decrease in $CMRO_2$ with hypercapnia.

Supplementary Material

Refer to Web version on PubMed Central for supplementary material.

ACKNOWLEDGMENT

We thank Kelly McCabe Gillen, PhD, for her assistance in manuscript editing.

References

1. Derdeyn CP, Yundt KD, Videen TO, Carpenter DA, Grubb RL Jr., Powers WJ. Increased oxygen extraction fraction is associated with prior ischemic events in patients with carotid occlusion. Stroke 1998;29(4):754–758. [PubMed: 9550507]
2. Yamauchi H, Fukuyama H, Nagahama Y, Nabatame H, Ueno M, Nishizawa S, Konishi J, Shio H. Significance of increased oxygen extraction fraction in five-year prognosis of major cerebral arterial occlusive diseases. Journal of nuclear medicine : official publication, Society of Nuclear Medicine 1999;40(12):1992–1998.
3. Derdeyn CP, Videen TO, Yundt KD, Fritsch SM, Carpenter DA, Grubb RL, Powers WJ. Variability of cerebral blood volume and oxygen extraction: stages of cerebral haemodynamic impairment revisited. Brain 2002;125(Pt 3):595–607. [PubMed: 11872616]
4. Gupta A, Chazen JL, Hartman M, Delgado D, Anumula N, Shao H, Mazumdar M, Segal AZ, Kamel H, Leifer D, Sanelli PC. Cerebrovascular reserve and stroke risk in patients with carotid stenosis or occlusion: a systematic review and meta-analysis. Stroke 2012;43(11):2884–2891. [PubMed: 23091119]
5. Ito M, Lammertsma AA, Wise RJS, Bernardi S, Frackowiak RSJ, Heather JD, McKenzie CG, Thomas DGT, Jones T. Measurement of regional cerebral blood flow and oxygen utilisation in patients with cerebral tumours using 15O and positron emission tomography: Analytical techniques and preliminary results. Neuroradiology 1982;23(2):63–74. [PubMed: 6979003]
6. Ishii K, Kitagaki H, Kono M, Mori E. Decreased medial temporal oxygen metabolism in Alzheimer's disease shown by PET. Journal of nuclear medicine : official publication, Society of Nuclear Medicine 1996;37(7):1159–1165.
7. He X, Yablonskiy DA. Quantitative BOLD: mapping of human cerebral deoxygenated blood volume and oxygen extraction fraction: default state. Magn Reson Med 2007;57(1):115–126. [PubMed: 17191227]
8. Yablonskiy DA, Sukstanskii AL, He X. BOLD-based Techniques for Quantifying Brain Hemodynamic and Metabolic Properties – Theoretical Models and Experimental Approaches. NMR in biomedicine 2013;26(8):963–986. [PubMed: 22927123]

9. Bolar DS, Rosen BR, Sorensen A, Adalsteinsson E. QUantitative Imaging of eXtraction of oxygen and TIssue consumption (QUIXOTIC) using venular-targeted velocity-selective spin labeling. Magnetic resonance in medicine 2011;66(6):1550–1562. [PubMed: 21674615]
10. Davis TL, Kwong KK, Weisskoff RM, Rosen BR. Calibrated functional MRI: mapping the dynamics of oxidative metabolism. Proc Natl Acad Sci U S A 1998;95(4):1834–1839. [PubMed: 9465103]
11. Hoge RD. Calibrated FMRI. NeuroImage 2012;62(2):930–937. [PubMed: 22369993]
12. Gauthier CJ, Hoge RD. Magnetic resonance imaging of resting OEF and CMRO2 using a generalized calibration model for hypercapnia and hyperoxia. NeuroImage 2012;60(2):1212–1225. [PubMed: 22227047]
13. Blockley NP, Griffeth VE, Simon AB, Buxton RB. A review of calibrated blood oxygenation level-dependent (BOLD) methods for the measurement of task-induced changes in brain oxygen metabolism. NMR in biomedicine 2013;26(8):987–1003. [PubMed: 22945365]
14. Jain V, Langham MC, Wehrli FW. MRI Estimation of Global Brain Oxygen Consumption Rate. Journal of Cerebral Blood Flow & Metabolism 2010;30(9):1598–1607. [PubMed: 20407465]
15. Wehrli FW, Fan AP, Rodgers ZB, Englund EK, Langham MC. Susceptibility-based time-resolved whole-organ and regional tissue oximetry. NMR in biomedicine 2017;30(4).
16. Fan AP, Benner T, Bolar DS, Rosen BR, Adalsteinsson E. Phase-based regional oxygen metabolism (PROM) using MRI. Magn Reson Med 2012;67(3):669–678. [PubMed: 21713981]
17. Fan AP, Bilgic B, Gagnon L, Witzel T, Bhat H, Rosen BR, Adalsteinsson E. Quantitative oxygenation venography from MRI phase. Magnetic resonance in medicine 2014;72(1):149–159. [PubMed: 24006229]
18. Kudo K, Liu T, Murakami T, Goodwin J, Uwano I, Yamashita F, Higuchi S, Wang Y, Ogasawara K, Ogawa A, Sasaki M. Oxygen extraction fraction measurement using quantitative susceptibility mapping: Comparison with positron emission tomography. Journal of cerebral blood flow and metabolism : official journal of the International Society of Cerebral Blood Flow and Metabolism 2016;36(8):1424–1433.
19. Zhang J, Liu T, Gupta A, Spincemaille P, Nguyen TD, Wang Y. Quantitative mapping of cerebral metabolic rate of oxygen (CMRO2) using quantitative susceptibility mapping (QSM). Magnetic Resonance in Medicine 2015;74(4):945–952. [PubMed: 25263499]
20. Zhang J, Cho J, Zhou D, Nguyen TD, Spincemaille P, Gupta A, Wang Y. Quantitative susceptibility mapping-based cerebral metabolic rate of oxygen mapping with minimum local variance. Magn Reson Med 2017.
21. Zhang J, Zhou D, Nguyen TD, Spincemaille P, Gupta A, Wang Y. Cerebral metabolic rate of oxygen (CMRO2) mapping with hyperventilation challenge using quantitative susceptibility mapping (QSM). Magnetic resonance in medicine 2017;77(5):1762–1773. [PubMed: 27120518]
22. Bulte DP, Kelly M, Germuska M, Xie J, Chappell MA, Okell TW, Bright MG, Jezzard P. Quantitative measurement of cerebral physiology using respiratory-calibrated MRI. NeuroImage 2012;60(1):582–591. [PubMed: 22209811]
23. Wang Y, Spincemaille P, Liu Z, Dimov A, Deh K, Li J, Zhang Y, Yao Y, Gillen KM, Wilman AH, Gupta A, Tsiouris AJ, Kovanlikaya I, Chiang GC, Weinsaft JW, Tanenbaum L, Chen W, Zhu W, Chang S, Lou M, Kopell BH, Kaplitt MG, Devos D, Hirai T, Huang X, Korogi Y, Shtilbans A, Jahng GH, Pelletier D, Gauthier SA, Pitt D, Bush AI, Brittenham GM, Prince MR. Clinical quantitative susceptibility mapping (QSM): Biometal imaging and its emerging roles in patient care. J Magn Reson Imaging 2017;46(4):951–971. [PubMed: 28295954]
24. Liu T, Spincemaille P, de Rochefort L, Wong R, Prince M, Wang Y. Unambiguous identification of superparamagnetic iron oxide particles through quantitative susceptibility mapping of the nonlinear response to magnetic fields. Magn Reson Imaging 2010;28(9):1383–1389. [PubMed: 20688448]
25. Ma Y, Sun H, Cho J, Mazerolle EL, Wang Y, Pike GB. Cerebral OEF quantification: A comparison study between quantitative susceptibility mapping and dual-gas calibrated BOLD imaging. Magnetic resonance in medicine 2020;83(1):68–82. [PubMed: 31373088]
26. Cho J, Kee Y, Spincemaille P, Nguyen TD, Zhang J, Gupta A, Zhang S, Wang Y. Cerebral metabolic rate of oxygen (CMRO2) mapping by combining quantitative susceptibility mapping

(QSM) and quantitative blood oxygenation level-dependent imaging (qBOLD). Magnetic resonance in medicine 2018;80(4):1595–1604. [PubMed: 29516537]

27. Cho J, Zhang S, Kee Y, Spincemaille P, Nguyen TD, Hubertus S, Gupta A, Wang Y. Cluster analysis of time evolution (CAT) for quantitative susceptibility mapping (QSM) and quantitative blood oxygen level-dependent magnitude (qBOLD)-based oxygen extraction fraction (OEF) and cerebral metabolic rate of oxygen (CMRO2) mapping. Magnetic resonance in medicine 2020;83(3):844–857. [PubMed: 31502723]
28. Xu B, Liu T, Spincemaille P, Prince M, Wang Y. Flow compensated quantitative susceptibility mapping for venous oxygenation imaging. Magn Reson Med 2014;72(2):438–445. [PubMed: 24006187]
29. Klassen LM, Menon RS. Optimal Phase Sensitive Combination of Multi-Channel, Multi-Echo Images. In Proceedings of the 21st Annual Meeting of ISMRM;Salt Lake City, USA, Abstract 3739.
30. Liu T, Wisnieff C, Lou M, Chen W, Spincemaille P, Wang Y. Nonlinear formulation of the magnetic field to source relationship for robust quantitative susceptibility mapping. Magnetic Resonance in Medicine 2013;69(2):467–476. [PubMed: 22488774]
31. Zhou D, Liu T, Spincemaille P, Wang Y. Background field removal by solving the Laplacian boundary value problem. NMR in biomedicine 2014;27(3):312–319. [PubMed: 24395595]
32. Liu Z, Spincemaille P, Yao Y, Zhang Y, Wang Y. MEDI+0: Morphology enabled dipole inversion with automatic uniform cerebrospinal fluid zero reference for quantitative susceptibility mapping. Magn Reson Med 2018;79(5):2795–2803. [PubMed: 29023982]
33. de Rochefort L, Liu T, Kressler B, Liu J, Spincemaille P, Lebon V, Wu J, Wang Y. Quantitative susceptibility map reconstruction from MR phase data using bayesian regularization: validation and application to brain imaging. Magn Reson Med 2010;63(1):194–206. [PubMed: 19953507]
34. Liu J, Liu T, de Rochefort L, Ledoux J, Khalidov I, Chen W, Tsiouris AJ, Wisnieff C, Spincemaille P, Prince MR, Wang Y. Morphology enabled dipole inversion for quantitative susceptibility mapping using structural consistency between the magnitude image and the susceptibility map. NeuroImage 2012;59(3):2560–2568. [PubMed: 21925276]
35. Wang Y, Liu T. Quantitative susceptibility mapping (QSM): Decoding MRI data for a tissue magnetic biomarker. Magn Reson Med 2015;73(1):82–101. [PubMed: 25044035]
36. Liu Z, Kee Y, Zhou D, Wang Y, Spincemaille P. Preconditioned total field inversion (TFI) method for quantitative susceptibility mapping. Magn Reson Med 2017;78(1):303–315. [PubMed: 27464893]
37. Spincemaille P, Liu Z, Zhang S, Kovanlikaya I, Ippoliti M, Makowski M, Watts R, de Rochefort L, Venkatraman V, Desmond P, Santin MD, Lehericy S, Kopell BH, Peran P, Wang Y. Clinical Integration of Automated Processing for Brain Quantitative Susceptibility Mapping: Multi-Site Reproducibility and Single-Site Robustness. J Neuroimaging 2019;29(6):689–698. [PubMed: 31379055]
38. Zhang Y, Brady M, Smith S. Segmentation of brain MR images through a hidden Markov random field model and the expectation-maximization algorithm. IEEE Trans Med Imaging 2001;20(1):45–57. [PubMed: 11293691]
39. Jenkinson M, Smith S. A global optimisation method for robust affine registration of brain images. Med Image Anal 2001;5(2):143–156. [PubMed: 11516708]
40. Jenkinson M, Bannister P, Brady M, Smith S. Improved optimization for the robust and accurate linear registration and motion correction of brain images. NeuroImage 2002;17(2):825–841. [PubMed: 12377157]
41. Woolrich MW, Ripley BD, Brady M, Smith SM. Temporal autocorrelation in univariate linear modeling of FMRI data. NeuroImage 2001;14(6):1370–1386. [PubMed: 11707093]
42. Worsley KJ. Ch14 Statistical Analysis of Activation Images. In: Jezzard P, Matthews PM, Smith SM, editors. Functional MRI: An introduction to methods: Oxford University Press Inc.; 2001.
43. Andersson JLR, Jenkinson M, Smith S. Non-linear registration aka Spatial normalisation. FMRIB Centre: Oxford; 2007.

44. Hoge RD, Atkinson J, Gill B, Crelier GR, Marrett S, Pike GB. Investigation of BOLD signal dependence on cerebral blood flow and oxygen consumption: the deoxyhemoglobin dilution model. Magn Reson Med 1999;42(5):849–863. [PubMed: 10542343]
45. Kosior RK, Lauzon ML, Steffenhagen N, Kosior JC, Demchuk A, Frayne R. Atlas-based topographical scoring for magnetic resonance imaging of acute stroke. Stroke 2010;41(3):455–460. [PubMed: 20093636]
46. Carpenter DA, Grubb RL Jr., Tempel LW, Powers WJ. Cerebral oxygen metabolism after aneurysmal subarachnoid hemorrhage. Journal of cerebral blood flow and metabolism : official journal of the International Society of Cerebral Blood Flow and Metabolism 1991;11(5):837–844.
47. Raichle ME, MacLeod AM, Snyder AZ, Powers WJ, Gusnard DA, Shulman GL. A default mode of brain function. Proceedings of the National Academy of Sciences 2001;98(2):676–682.
48. Fan AP, Schäfer A, Huber L, Lampe L, von Smuda S, Möller HE, Villringer A, Gauthier CJ. Baseline oxygenation in the brain: Correlation between respiratory-calibration and susceptibility methods. NeuroImage 2016;125:920–931. [PubMed: 26549301]
49. Mintun MA, Raichle ME, Martin WR, Herscovitch P. Brain oxygen utilization measured with O-15 radiotracers and positron emission tomography. Journal of nuclear medicine : official publication, Society of Nuclear Medicine 1984;25(2):177–187.
50. Ito H, Kanno I, Kato C, Sasaki T, Ishii K, Ouchi Y, Iida A, Okazawa H, Hayashida K, Tsuyuguchi N, Ishii K, Kuwabara Y, Senda M. Database of normal human cerebral blood flow, cerebral blood volume, cerebral oxygen extraction fraction and cerebral metabolic rate of oxygen measured by positron emission tomography with 15O-labelled carbon dioxide or water, carbon monoxide and oxygen: a multicentre study in Japan. European Journal of Nuclear Medicine and Molecular Imaging 2004;31(5):635–643. [PubMed: 14730405]
51. Godoy DA, Seifi A, Garza D, Lubillo-Montenegro S, Murillo-Cabezas F. Hyperventilation Therapy for Control of Posttraumatic Intracranial Hypertension. 2017;8(250).
52. Chen JJ, Pike GB. Global cerebral oxidative metabolism during hypercapnia and hypocapnia in humans: implications for BOLD fMRI. Journal of cerebral blood flow and metabolism : official journal of the International Society of Cerebral Blood Flow and Metabolism 2010;30(6):1094–1099.
53. Jain V, Langham MC, Floyd TF, Jain G, Magland JF, Wehrli FW. Rapid magnetic resonance measurement of global cerebral metabolic rate of oxygen consumption in humans during rest and hypercapnia. Journal of cerebral blood flow and metabolism : official journal of the International Society of Cerebral Blood Flow and Metabolism 2011;31(7):1504–1512.
54. Xu F, Uh J, Brier MR, Hart J Jr., Yezhuvath US, Gu H, Yang Y, Lu H. The influence of carbon dioxide on brain activity and metabolism in conscious humans. Journal of cerebral blood flow and metabolism : official journal of the International Society of Cerebral Blood Flow and Metabolism 2011;31(1):58–67.
55. Driver ID, Wise RG, Murphy K. Graded Hypercapnia-Calibrated BOLD: Beyond the Iso-metabolic Hypercapnic Assumption. Frontiers in Neuroscience 2017;11(276).
56. Chen JJ, Pike GB. MRI measurement of the BOLD-specific flow-volume relationship during hypercapnia and hypocapnia in humans. NeuroImage 2010;53(2):383–391. [PubMed: 20624474]
57. Aslan S, Xu F, Wang PL, Uh J, Yezhuvath US, van Osch M, Lu H. Estimation of labeling efficiency in pseudocontinuous arterial spin labeling. Magnetic resonance in medicine 2010;63(3):765–771. [PubMed: 20187183]

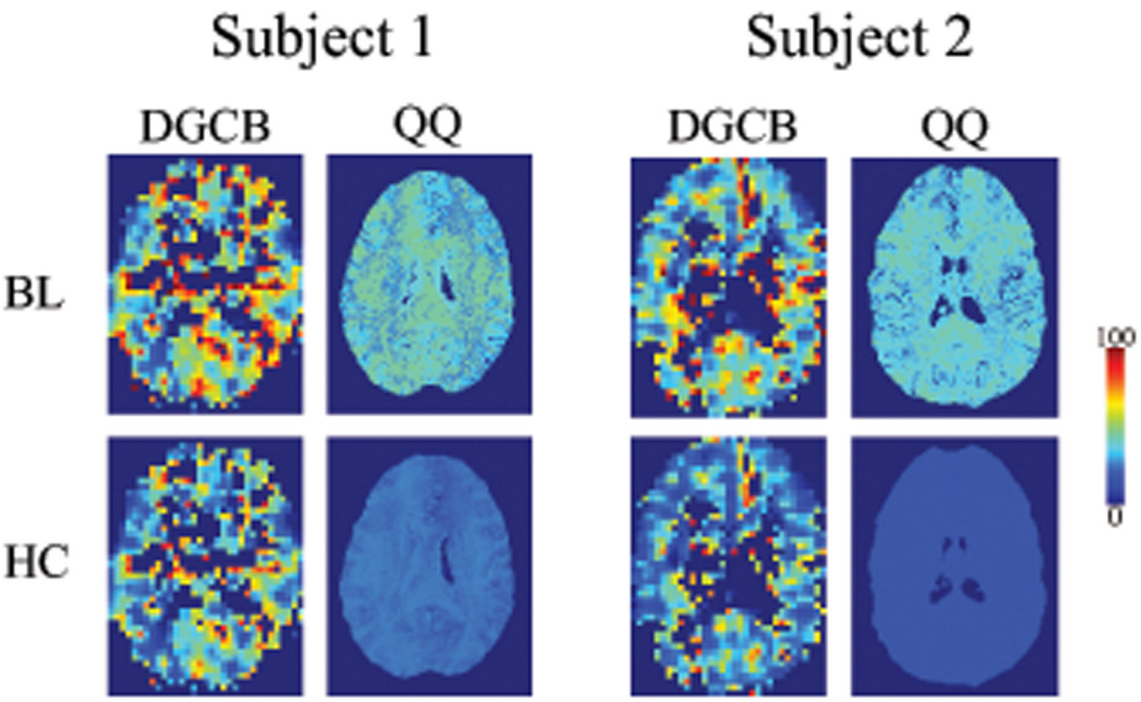

Figure 1.

OEF maps from DGCB and QQ between baseline (BL) and hypercapnia (HC) in two subjects. In DGCB, HC-OEF was estimated based on the iso-$CMRO_2$ assumption with BL-OEF, BL-CBF, and HC-CBF. QQ shows more uniform OEF than DGCB. Both QQ and DGCB shows decreased OEF in HC compared to BL. The unit of color scale is %. Results of all 10 subjects are illustrated in Supporting Information Figures S1 and S2.

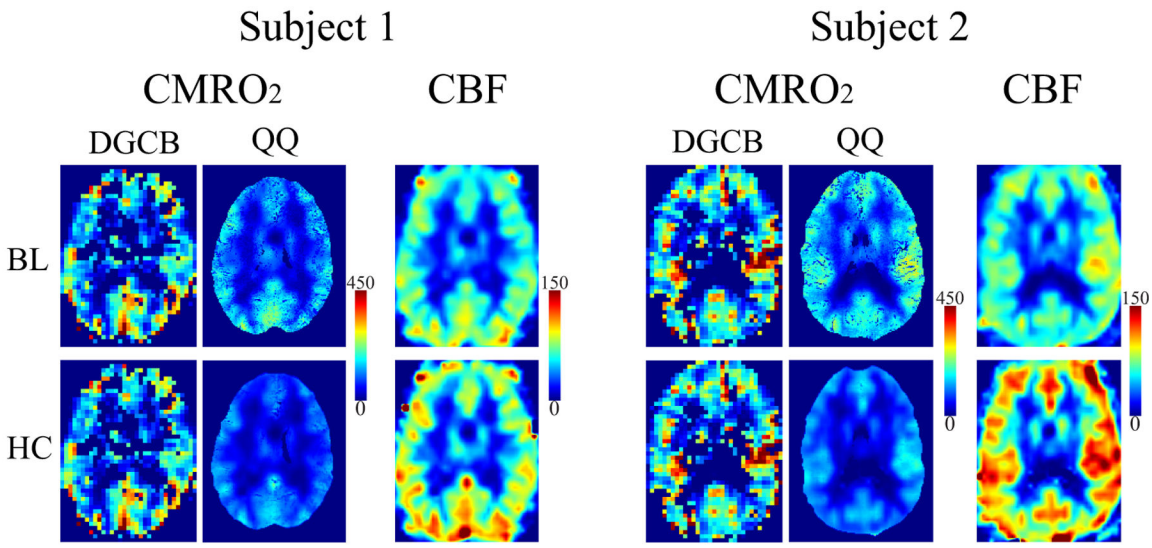

Figure 2.

$CMRO_2$ maps from DGCB and QQ and CBF maps between baseline (BL) and hypercapnia (HC) in the same two subjects as in Figure 1. QQ shows good $CMRO_2$ contrast between gray and white matter. QQ shows decreased $CMRO_2$ in HC compared to BL. Note that DGCB-CMRO2 in HC is identical to the one at BL (iso-$CMRO_2$ assumption). The BL-CBF was obtained by registering DGCB-CBF to QSM resolution. The HC-CBF was inferred based on the cerebrovascular reactivity (CVR) obtained from DGCB during hypercapnia and $PetCO_2$ obtained from QSM during hypercapnia. The unit of color scale is μmol O_2/min/100g for $CMRO_2$ and ml/min/100g for CBF. Results of all 10 subjects are illustrated in Supporting Information Figures S1 and S2.

Table 1.

Average and standard deviation of OEF and $CMRO_2$ in CGM. The unit of OEF and $CMRO_2$ is % and μmol O_2/min/100g, respectively. BL and HC indicate baseline and hypercapnia, respectively.

	OEF				CMRO2		
	DGCB		QQ		DGCB	QQ	
Subject #	BL	HC	BL	HC	BL=HC	BL	HC
1	48.9 ± 18.6	38.6 ± 16.6	35.2 ± 8.0	21.7 ± 3.2	189.7 ± 82.7	134.5 ± 38.6	101.7 ± 23.0
2	42.5 ± 16.8	30.2 ± 14.6	33.5 ± 7.6	16.9 ± 1.7	195.7 ± 88.7	151.6 ± 43.3	109.4 ± 24.0
3	26.7 ± 14.9	20.3 ± 13.2	36.1 ± 6.9	22.1 ± 3.6	121.4 ± 79.6	162.1 ± 48.8	143.5 ± 40.9
4	31.0 ± 13.2	22.4 ± 12.0	44.6 ± 10.5	29.2 ± 5.7	134.8 ± 76.3	191.1 ± 66.4	164.7 ± 49.3
5	28.6 ± 11.6	20.1 ± 10.3	32.1 ± 5.6	16.9 ± 3.0	125.8 ± 63.5	136.9 ± 36.3	112.7 ± 31.4
6	34.7 ± 16.0	26.7 ± 14.7	44.3 ± 10.4	23.4 ± 4.0	125.6 ± 68.3	160.2 ± 48.6	152.3 ± 47.6
7	52.7 ± 17.9	40.0 ± 16.3	43.3 ± 10.7	20.8 ± 1.8	259.7 ± 105.3	211.2 ± 63.9	128.6 ± 24.8
8	44.0 ± 16.8	34.0 ± 15.8	25.8 ± 6.7	17.0 ± 2.9	211.0 ± 100.0	121.8 ± 38.5	97.8 ± 38.0
9	29.6 ± 14.2	20.5 ± 12.6	28.5 ± 5.4	14.7 ± 2.7	96.6 ± 61.3	93.6 ± 27.2	71.2 ± 25.3
10	41.0 ± 14.8	31.2 ± 13.8	31.3 ± 7.3	24.2 ± 5.7	221.9 ± 92.4	168.0 ± 47.9	182.5 ± 54.8
avg ± std	38.0 ± 9.1	28.4 ± 7.6	35.5 ± 6.7	20.7 ± 4.4	168.2 ± 54.1	153.1 ± 33.8	126.4 ± 34.2

Table 2.

Average of CBF, CVR, and *v* in CGM. The unit of CBF, CVR, and *v* is ml/min/100g, Δ%CBF/mmHg $PetCO_2$, and %, respectively. The baseline CBF was acquired in DGCB, then registered to QSM resolution. BL and HC indicate baseline and hypercapnia, respectively. The HC-CBF was inferred based on the cerebrovascular reactivity (CVR) from DGCB during hypercapnia and $PetCO_2$ obtained from QSM during hypercapnia, respectively. BL-*v* and HC-*v* maps are shown in Supporting Information Figure S3.

Subject #	BL-CBF DGCB=QQ	CVR	HC-CBF DGCB	HC-CBF QQ	BL-*v* QQ	HC-*v* QQ
1	62.8 ± 11.9	4.3	85.2 ± 17.2	79.7 ± 13.6	3.0 ± 0.5	3.3 ± 0.7
2	61.9 ± 12.0	7.0	94.2 ± 20.9	90.6 ± 17.8	3.0 ± 0.5	3.5 ± 0.7
3	55.1 ± 14.1	8.0	78.6 ± 20.5	83.9 ± 20.9	3.0 ± 0.6	3.2 ± 0.6
4	54.0 ± 14.2	10.0	79.8 ± 21.5	74.0 ± 17.6	2.8 ± 0.8	2.6 ± 0.6
5	49.7 ± 10.5	8.9	76.7 ± 18.1	79.5 ± 17.4	3.5 ± 0.3	3.4 ± 0.7
6	47.2 ± 10.1	9.0	66.3 ± 15.4	88.6 ± 23.2	2.0 ± 0.5	3.1 ± 0.8
7	66.5 ± 12.5	5.2	93.5 ± 18.1	87.6 ± 15.4	2.1 ± 0.5	3.7 ± 0.6
8	59.8 ± 12.2	5.6	82.7 ± 17.9	75.3 ± 24.6	2.9 ± 0.4	3.1 ± 0.6
9	39.0 ± 9.8	8.0	60.8 ± 18.1	60.6 ± 17.6	3.1 ± 0.2	2.9 ± 0.7
10	71.9 ± 13.4	7.3	101.3 ± 19.9	104.7 ± 19.9	2.9 ± 0.4	1.9 ± 0.4
avg ± std	56.8 ± 9.8	7.3 ± 1.8	81.9 ± 12.5	82.4 ± 11.8	2.8 ± 0.4	3.1 ± 0.5